# Internal Insulation and Corrosion Control of Molten Chloride Thermal Energy Storage Tanks

Samuel H. Gage[1], Josh J. Bailey[2], Donal P. Finegan[1], Dan J. L. Brett[2], Paul R. Shearing[2], Craig S. Turchi[1]

[1]*National Renewable Energy Laboratory, 15013 Denver West Parkway, Golden, CO 80401, USA.*
[2]*Electrochemical Innovation Lab, Department of Chemical Engineering, University College London, London WC1E 7JE, UK.*

** corresponding author: Samuel.Gage@nrel.gov*

**Abstract.** A chloride-based molten-salt system that uses a ternary blend of $MgCl_2$/KCl/NaCl is investigated to provide higher-temperature thermal energy storage capability than conventional nitrate salt-based systems. Despite their high thermal stability and operating temperature, molten chlorides present several challenges, including the design of internal liners to prevent the corrosion and thermal stress of alloy tank shells. This work discusses issues and potential solutions related to containment of molten chloride salt, specifically the optimization of the hot face refractory materials for use as internal liners. Three down-selected refractory materials were analyzed with respect to permeation of salt through the material as well as chemical stability during high temperature operation. Through the application of X-ray imaging and electron spectroscopy techniques, highly stable secondary surface phases in equilibrium with the molten salt were identified, as well as time-dependent changes in the salt composition itself.

## Introduction

The U.S. Department of Energy Generation 3 (DOE Gen3) program seeks to develop higher efficiency concentrating solar power (CSP) plants equipped with thermal energy storage (TES) that can provide cost-competitive, flexible power for the U.S. electricity grid. The Gen3 Liquid Pathway CSP plant closely resembles the configuration of current molten salt power towers with two-tank thermal storage, as shown in Figure 1. This system aims to deliver greater efficiency over current state-of-the-art nitrate salt CSP plants, by utilizing a molten salt with greater thermal stability and an advanced supercritical carbon dioxide ($sCO_2$) Brayton power cycle.[1] Nitrate salt thermally decomposes above 565 °C, whereas the target ternary chloride blend ($MgCl_2$/KCl/NaCl) offers thermal stability above 800 °C.[1] The increased operating temperature however imposes constraints on the materials that can be used in TES tank construction. The hot salt tank is expected to contain salt at temperatures around 720 °C. The strength of stainless steel is compromised at these temperatures and is highly susceptible to corrosion by the molten chloride salt. Although nickel superalloys would be capable of withstanding the conditions, these materials are prohibitively expensive at scale.

To address these concerns, refractory ceramic-based containment materials are proposed to line the inside of TES storage tanks.[2] Refractory liners have been employed effectively in the magnesium industry, which electrolytically reduces molten chloride salt to produce metallic magnesium.[3] Internal insulation of these tanks allows carbon steel shells to be used, which represents significant cost savings over stainless steel alloys. The composition of the internal liner requires careful consideration to maximize the efficacy of multiple properties including corrosion resistance, inhibiting salt permeation, strength at operating temperature, durability, and cost. This is particularly true for the

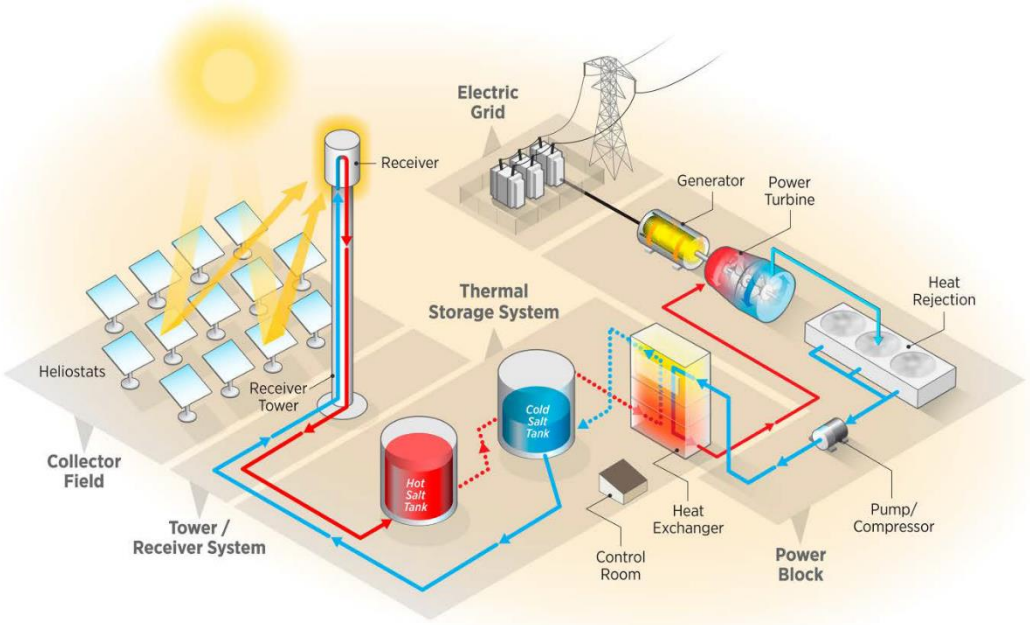


**Figure 1.** Schematic of Gen3 Liquid Pathway CSP plant with power tower and two-tank storage

material at the interface with the salt, known as the hot face, which is responsible for protecting the insulating layers between the tank shell wall and the hot face layer.

The salt in both the hot and cold tanks (720 °C and 500 °C, respectively) is expected to be above the freeze temperature of the ternary chloride blend (400 °C). Due to the operating temperatures, it is not expected that a freeze plane will develop in the hot face. The hot face must therefore be designed to withstand chemical corrosion and inhibit permeation of molten salt into the insulating layers.

Anticorrosion measures are an active topic of research in molten salt thermal storage. The tested strategies include pre-oxidation, atmosphere control in a closed tank, graphitization, and nanoparticles.[4,5] The surface passivation of alloys by forming a protective ceramic layer has also been proven effective at mitigating corrosion induced by both the liquid and vapor phases of molten chlorides. Surface layers such as $Al_2O_3$, yttria-stabilized zirconia (YSZ), and metallic nickel-based alloys have been successful at inhibiting the diffusion of chromium and the penetration of salt into the alloys.[6,7] In a similar fashion, passive corrosion of refractories is also known to occur. Corrosion reaction products in refractories, which are solid phase and adherent to the refractory surface, may act to reduce the overall rate of corrosion by inhibiting further permeation of the melt into the refractory (i.e. passive corrosion).[8,9] Examples of passive corrosion include the formation of a dense MgO layer in MgO-graphite refractories[10] and of a $MgAl_2O_4$ spinel layer in the corrosion of Mg-$Al_2O_3$ refractories by steel slags[11], both of which have been shown to resist slag penetration into the material.

Molten salts are a well-established reaction media for the production of ceramic powders.[12,13] Molten chloride salts in particular have been used to synthesize complex magnesium-rich ceramics, such as cordierite and forsterite.[14–17] Passivating corrosion

layers that are rich in magnesium have been observed at the salt/ceramic interface and decrease abruptly in concentration as a function of depth into the ceramic.[18] The formation of a secondary phase on a ceramic surface poses the risk of differential thermal expansion and cracking, but should the system be held isothermally without thermal cycling, ceramics such as forsterite, which are reported to have a high melting point (1890 °C), low thermal expansion, and good chemical stability, may inhibit salt permeation and corrosion as in ceramic-coated alloys.[19,20]

Herein, the corrosion behavior of hot face refractory candidates is studied in the ternary chloride salt blend, $MgCl_2$/KCl/NaCl. Based on industrial standards, refractory cup and coupon tests are performed to down-select the ideal candidate. This refractory is then subjected to long-duration chemical compatibility tests in molten chloride salt, whereupon examination of the salt/refractory interface is performed with electron microscopy, bulk properties are characterized with X-ray techniques and mechanical testing, and the internal microstructure is imaged with X-ray Computed Tomography (CT). The effect of long-term materials testing on the thermophysical properties of the salt is also discussed. The formation of a secondary ceramic phase at the refractory surface is reported and speculated to inhibit the permeation of molten salt through the material bulk.

## Materials and Methods

Refractory materials were initially down-selected by examining salt corrosion in a machined refractory cup following procedures outlined in the Alcoa Cup Penetration experiment.[21] Cups were machined nominally to 75 mm width and height, with a nominal cup cavity of 50 mm width and height. Long-duration chemical compatibility of refractories was performed by fully immersing refractory “coupons” in molten salt inside a quartz crucible under static conditions, according to guidelines documented in ASTM C621-09 (Standard Test Method for Isothermal Corrosion Resistance of Refractories to Molten Glass).[22] Cuboidal refractory coupons were cut with the approximate dimensions of 13 mm × 13 mm × 5 mm. Experiments with coupons were conducted in triplicate. The ternary chloride salt was purified prior to all experiments according to a previously reported procedure.[23] The protocol adds a small amount of additional halite (65 g halite per 1 kg of anhydrous carnallite) to commercial anhydrous carnallite to provide the desired ternary blend (nominally 40/40/20 mol% $MgCl_2$/KCl/NaCl).[24]

All sample preparation was performed inside an inert glovebox and transportation of materials to and from the furnace vessel was done within 5 minutes to minimize exposure of samples to the atmosphere. The test vessel, shown in Figure 2, was sealed to atmosphere and heated inside a crucible furnace. The vessel cap was fitted with a gas inlet and outlet to maintain a constant nitrogen purge (approximately 100 mL $min^{-1}$), as well as a K-type thermocouple to measure temperature. A refractory lid was placed over the sample crucible to minimize the introduction of contaminants from the environment to the system.

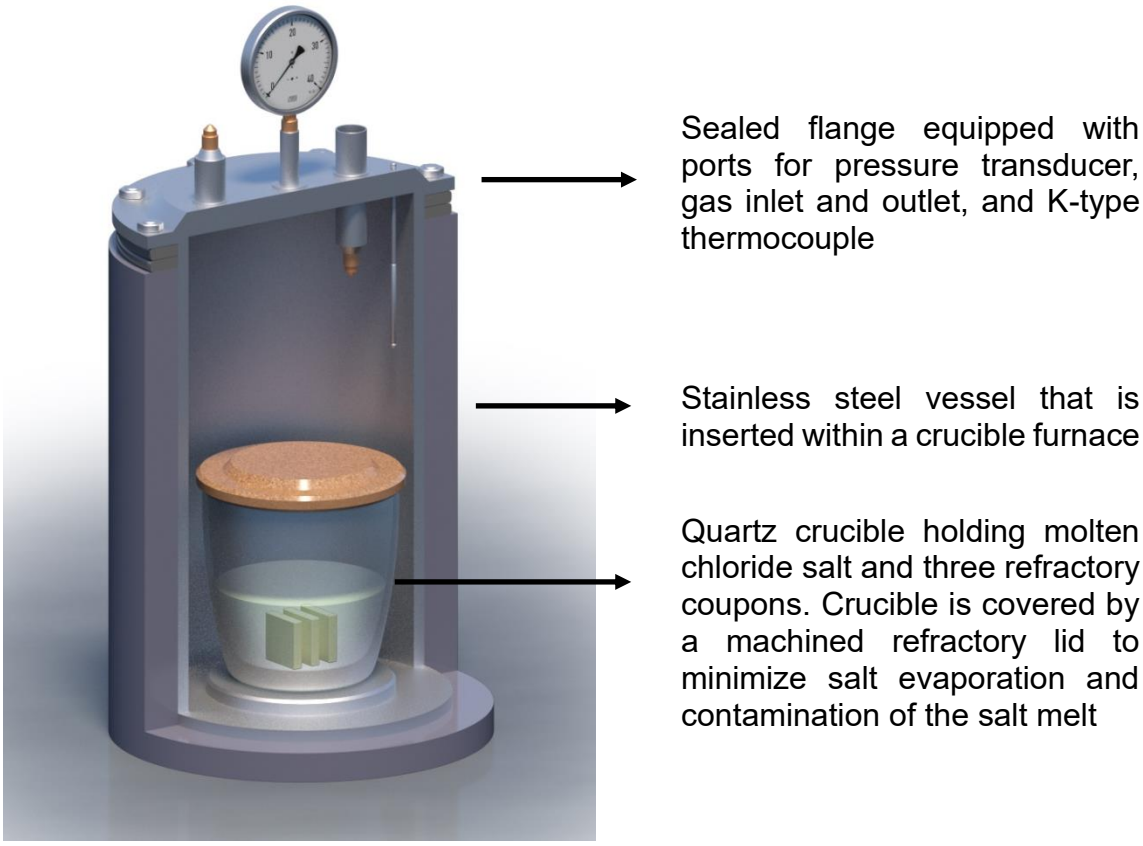


**Figure 2.** Cutaway of the experimental setup of refractory compatibility testing. Refractories are cut into three coupons with nominal dimensions of 13 mm x 13 mm x 5 mm and fully immersed in purified chloride salt within a quartz crucible. The crucible is covered with a refractory lid. The vessel is sealed with a cap equipped nitrogen inlet and outlet port, a pressure transducer, and a K-type thermocouple.

Once sealed the vessel was evacuated to 0.8 bar before being filled with nitrogen. This process was repeated three times. The vessel was then purged at a constant 100 mL $min^{-1}$ for approximately 30 min prior to beginning the heating schedule. The sample was heated to 120 °C and held for 2 hours to remove any residual water. The heating was increased at 2 °C $min^{-1}$ to a sample temperature of 720 °C and held isothermally for a given amount of time. After completion of the experiment, the furnace was cooled at 2 °C $min^{-1}$ to room temperature. The entire quartz crucible, with the frozen block of salt inside, was transferred entirely to the inert glovebox. The crucible was broken, and the salt block was picked apart by hand, or if necessary carefully with hammer and chisel. The coupons were not washed with water to retain the penetrated salt. Rather the coupon was lightly polished with SiC abrasive paper to remove excess salt. Until needed for follow-on experiments and characterization, coupons were sealed in vacuum packaging or stored in the inert glovebox to prevent any oxidation of the samples.

Samples were visually examined for cracks, spalling, structural integrity of the refractory, and discoloration. One coupon was placed in an ultrasonic water bath to remove as much salt as possible. This sample was used for X-ray diffraction (XRD) using a Rigaku DMax instrument before and after exposure to the salt. A second refractory coupon was cross-sectioned for microscopy analysis. Using a diamond saw, the coupon was cut about

6–7 mm from the short edge. The cross-sectioned surface was then mounted in phenolic resin and polished for analysis using 80 grit coarse polish, followed by 800 grit fine polish. Again, polishing was performed in the absence of water or other liquid polishing compounds to inhibit loss of permeated salt. The mounted coupons were sputtered with a 10-nm layer of palladium/gold to increase conductivity. The cross-sections were then analyzed with scanning electron microscopy and energy-dispersive X-ray spectroscopy (SEM/EDS). SEM was performed using a Hitachi 4800 SEM and provided high-resolution imaging of the refractory surface, particularly the corrosion interface. This was paired with EDS to provide chemical information for regions of interest in the sample.

The Sonoscan Gen5 C-Mode Scanning Acoustic Microscope (C-SAM) was used to inspect refractories for defects before and after salt exposure. The ultrasound frequencies are capable of detecting defects, such as voids, cracks, and delaminated layers of entire samples at a fraction of the time compared to SEM. Whole surfaces of the coupons were examined with a 50 MHz, 12.7-mm focal length transducer, capable of achieving a resolution of 52 µm.

The compressive strength was measured using a uniaxial screw-driven compression instrument (Instron 1125), equipped with a 5000-N load cell. The high cold crush strength (CCS) of these refractories required the machining of very small specimens to reach the forces required to test the material to its failure point. Refractory coupons were immersed in molten chloride salt for 3000 hours and machined to 5 mm x 5 mm specimens for mechanical testing. The test protocol followed guidelines outlined by ASTM Standard C-133 (Standard Test Methods for Cold Crushing Strength and Modulus of Rupture of Refractories).[25] The specimens were placed under load with a compressive extension of 0.2 mm $min^{-1}$. Failure was defined as a ≥ 40% loss of compressive force.

X-ray micro-CT of approximately cubic pieces (dimensions of ~14 mm) of refractory liner was conducted using a Nikon XT H 225 instrument with an X-ray beam voltage of 132 kV and beam power of 12 W. By purely geometrical magnification, a voxel size of 10.0 µm was achieved. 3176 projections, each at 1-s exposure time, gave an overall scan time of ~ 1 hour. Reconstruction of the radiographic projections into a 3D tomogram was performed in CTPro3D (Nikon). Image processing and analysis was carried out either in Avizo (Thermo Fisher Scientific) or Dragonfly (Object Research Systems).

Raw images were first shading corrected, before being Gaussian-filtered (3D, kernel size of 4) and segmented using a standard watershed segmentation approach.[26] Phase fraction and surface area calculations were conducted by simple voxel counting procedures whereas penetration depth was calculated using the following approach. Pores that connected to each of the six faces of the analyzed volume were isolated separately and their furthermost point from the face in question identified. The perpendicular distance from these points to the face were plotted for each direction for both samples. Exemplar volume renderings from three orthogonal faces of each hot face material were also generated to visualize the porous network extent, as shown in Figure 6.

## Results and Discussion

The role of the liner's hot face layer is to protect the underlying insulating layers. Three refractory candidates were studied based on knowledge of successful aluminosilicate hot

face materials used in the magnesium electrolysis industry.[3] Refractory candidates that were most similar to the industrial brick based on physical and chemical properties are detailed in Table 1 and labeled as hot face A, B, and C.

The reaction interface of the molten salt and hot face material must be understood to devise a strategy to inhibit salt permeation and wetting of the insulating layer. The initial down-selection of hot face candidates was completed by performing a refractory cup test. The cups were machined to the dimensions shown in Figure 3. The cup was charged with purified salt, heated to 720 °C, and held for 100 hours at that temperature under nitrogen atmosphere. Only hot face A and B had salt remaining in the cup after completion of the test. The salt completely permeated into hot face C. It should be noted that hot face A and B have lower open porosity than hot face C (8%, 6%, and 16%, respectively), which likely contributed to the retention of salt within the hot face A and B cups.

**Table 1.** Hot face candidates with similar physical and chemical properties to the industrial reference brick

| **Composition (%)** | **Hot Face A** | **Hot Face B** | **Hot Face C** | **Industry Reference** |
|---|---|---|---|---|
| **$Al_2O_3$** | 28.0 | 49.0 | 42.6 | 38.3 |
| **$SiO_2$** | 66.4 | 48.0 | 52.2 | 56.7 |
| **MgO** | 1.7 | n/a | 0.3 | 0.3 |
| **$Fe_2O_3$** | 0.4 | 1.4 | 1.4 | 1.6 |
| **CaO** | 0.4 | n/a | 0.2 | 0.3 |
| **$TiO_2$** | 1.7 | n/a | 2.3 | 1.7 |
| **$Na_2O$ and $K_2O$** | 2.6 | n/a | 0.9 | 0.9 |
| **Porosity (%)** | 8.0 | 6.0 | 15.7 | 10 |
| **Density (g $cm^{-3}$)** | 2.32 | 2.55 | 2.26 | 2.32 |
| **Thermal Conductivity (W $m^{-1}$ $K^{-1}$), 650-800 °C** | 1.37 | 1.95 | 1.31 | n/a |

All cups were cross-sectioned and examined for structural soundness. None of the cups exhibited signs of structural damage (e.g. crumbling or flaking) in the areas exposed to the salt. A portion of the cup cavity was cross-sectioned for SEM/EDS analysis. Figure 3 shows the chlorine EDS map of each material. The salt/refractory interface is located at the top of the image, with the bulk of the specimen extending downward. A clear depiction of the salt permeation observed in hot face C is seen in the Cl map, as extensive salt penetration is observed into the material bulk. Both hot face A and B retard salt permeation into the material, however isolated regions of salt contamination are seen throughout the bulk of hot face B. It was hypothesized that hot face B had connected porosity which allowed molten salt to be transported from the surface into the bulk of the material. In hot face A, very little salt permeated into the material bulk which could be due to low connectivity of surface connected pores to the material bulk and/or a secondary phase forming at the opening of said pores that prevents molten salt ingress.

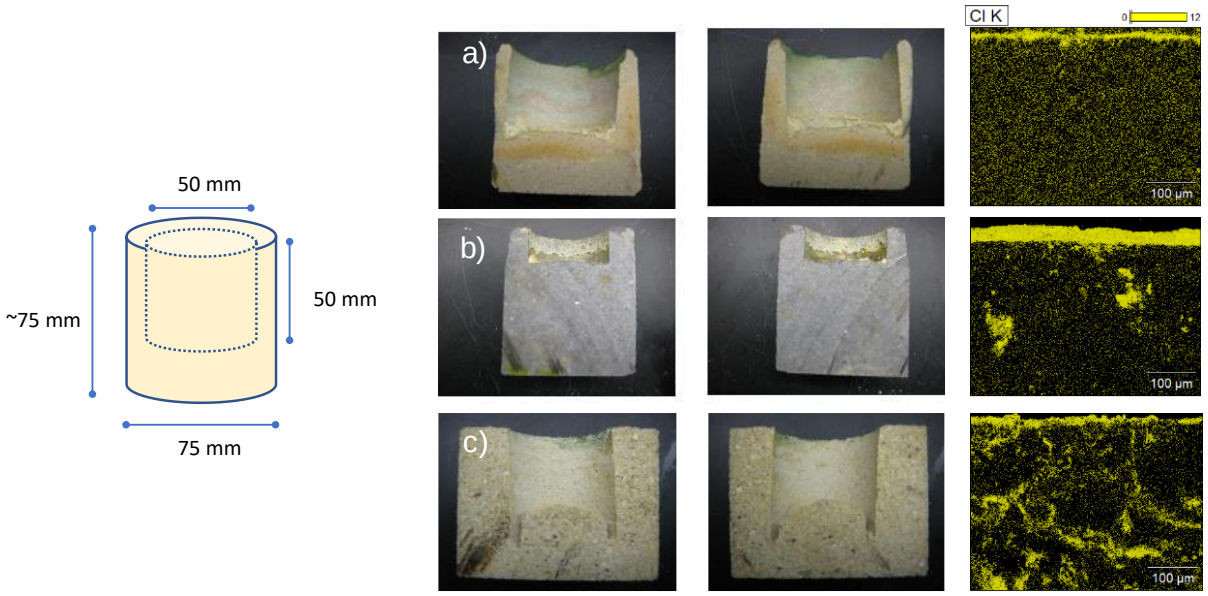


**Figure 3.** Sectioned cup tests after 100-hour salt exposure. Cup dimensions shown on the left. Sectioned cups of hot face A (a), hot face B (b), and hot face C (c), with EDS map showing presence of chlorine where the top of the EDS image was the surface in contact with the salt.

In order to inspect the internal microstructures of hot face A and B and to test the hypothesis that a secondary phase formed only at the surface of hot face A and thus prevented salt ingress, X-ray CT of the materials (both virgin and immersed in molten salt) was carried out. Large volumes were investigated at a voxel size of 10.0 µm, to evaluate in three dimensions, the ingress of molten salt into the porous networks of each material. Single tomographic slices of hot face A and B are presented in Figure S1 and Figure S2, respectively, with processed versions, binary and (where applicable) ternary segmentations.

Qualitatively it is clear, not just from the single orthoslices in Figures S1 and S2 but across the entire tomograms, that salt ingress is significant in hot face B but almost negligible in hot face A. However, due to the high grayscale inclusions in the hot face A refractory, quantitative determination of the extent of salt ingress is less clear-cut than in the case of hot face B where all high grayscale material can be assumed to represent ingressed molten salt. Table S1 displays instructive metrics extracted from the binary and ternary segmentations of both hot face A and B.

The pore network volume in hot face B that had not been immersed is found by X-ray CT to be significantly larger than that which remains unfilled in the immersed sample (~38% filling based on the assumption of the same initial pore phase fraction). This matches what is evident from the tomograms. There is salt that has ingressed right into the bulk of the specimen. This is further illustrated in Figure 4 which shows a slice-by-slice analysis of phase fraction for hot face B in each of the orthogonal directions. This contrasts with the case of hot face A, which does not appear to show qualitative or quantitative evidence of significant salt ingress. Having segmented the high grayscale inclusions in the “not immersed” sample, and assuming a similar composition in the “immersed” sample,

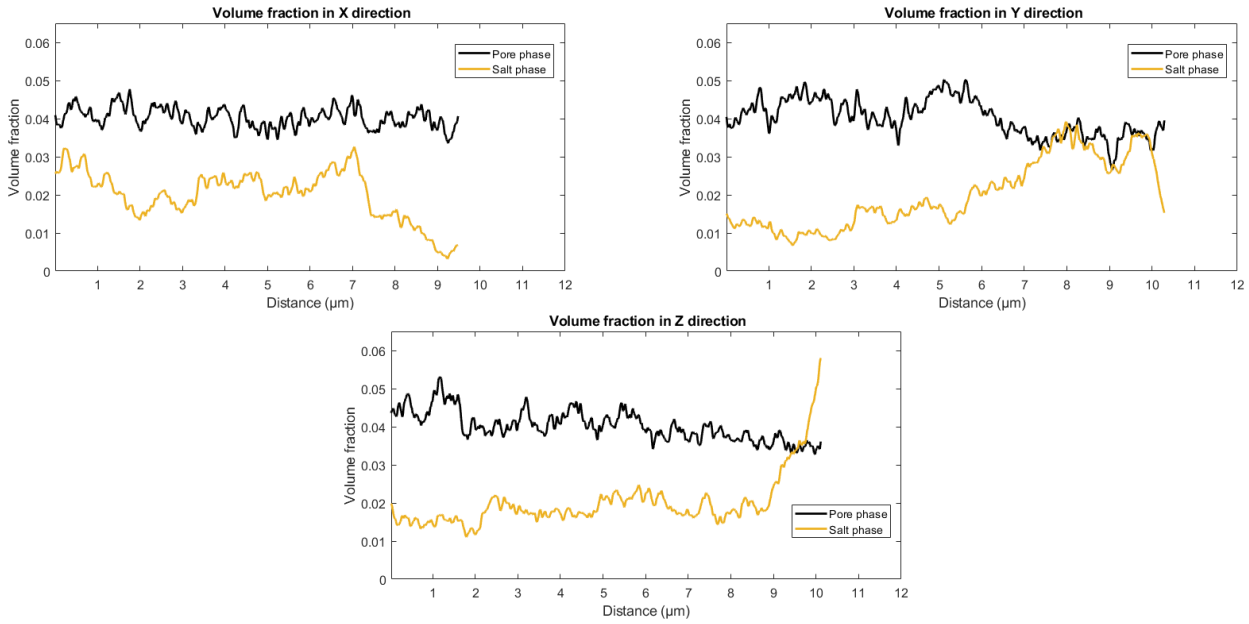


**Figure 4.** Slice-by-slice analysis of hot face B, showing that the salt phase is present throughout the bulk refractory material

implies approximately ~7% original pore network is attributable to ingressed salt. This matches with the observation that there are some thin, high-grayscale sinuous networks evident towards the surface after immersion in molten salt, but these are not apparent in the native sample. Moreover, this qualitatively matches the aforementioned SEM/EDS result.

The X-ray CT images demonstrated that there were porous networks connected to the surface of the analyzed volume (very close to the actual sample surface) in both cases. This analysis also highlighted that although the pore phase fraction of hot face B matched the manufacturer's specifications, that for hot face A was significantly less (by 50 %) than nominally specified. This may suggest that there are finer pore networks beneath the resolution used here. At the imaged resolution, the area of the porous network at the surface of the imaged volumes for hot face A and B were ~57.0 and ~46.4 $mm^2$, respectively, suggesting a greater potential for salt ingress in hot face A if all other factors are equal. However, further analysis of the depth penetration of the pore networks in each case (Figure 5) highlighted the difference in the nature of the porosity and explained the lack of salt ingress to the bulk of hot face A.

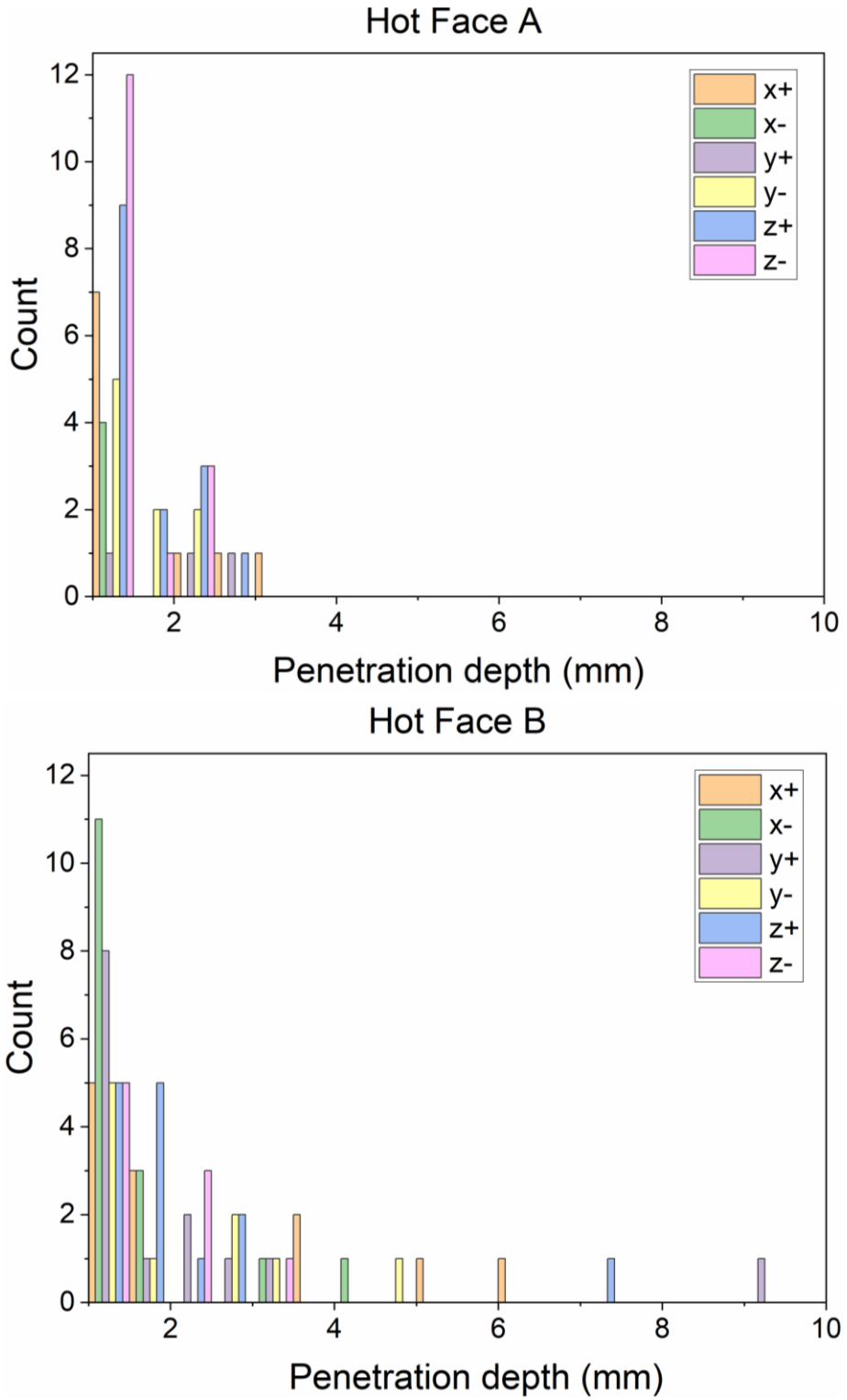


**Figure 5.** Penetration depth analysis for hot face A and B, based on the perpendicular distance of the most penetrated point of each porous network relative to each face of analyzed volume. Although hot face A had slightly higher pore area at the surface, the pore network does not penetrate far into the brick.

Although most surface-connected pores in both materials only penetrated approximately 250 µm or less from the surface, there was a clear distinction between the penetration

depth distribution of the networks of larger pore volume. For hot face A, the maximum penetration depth was ~3 mm, with only 57 porous networks with a penetration depth above 1 mm (from any single face), whereas the maximum penetration depth for hot face B was >9 mm, with 75 porous networks above 1 mm. This quantification indicates that there is far greater connectivity between the surface of hot face B and its bulk than is the case for hot face A, which explains why the same treatment led to a greater penetration of molten salt for hot face B than hot face A. The penetration observed via X-ray CT in hot face A is more likely due to native surface cracks, which leads to permeation of salt into the void spaces as seen in Figure S3. Although these inherent cracks were seldom observed in SEM-EDS, the character of the porous networks seen in hot face A would nonetheless suggest a greater degree of molten salt ingress than appears from both SEM-EDS and the semi-quantitative X-ray CT analysis, which supports the fact that formation of a secondary phase may be preventing as much penetration as might be expected from the accessible porosity. Figure 6 shows volume renderings of the surface-connected pores in both materials to further visualize the different character of the porous networks.

As a result of these analyses, hot face A became the focus of subsequent chemical compatibility testing. For long duration tests on hot face A, refractory coupons were cut and immersed in molten salt at 720 °C and analyzed according to the methods described above. Figure 7 shows the chlorine and magnesium EDS maps of the cross-sectional refractory/salt interface for all tested durations. The refractory/salt interface is at the top of the image, with the bulk of the material extending to the bottom. The data suggest that molten chloride salt does not penetrate deeply into the material. Salt penetration depth was measured by the depth of the chlorine signal in the specimen. Figure S4 plots the average measured penetration depth as a function of exposure time. The added trendline is used to extrapolate the penetration depth (Table S2). With the given rate, one can expect a penetration depth of 2.0 mm after 20 years and 2.9 mm after 30 years of continuous exposure. This is a very small fraction of the expected 114 to 230 mm brick thickness (based on standard 4.5-inch or 9-inch bricks). However, one must be cautious with such a large extrapolation of 3000-h data.

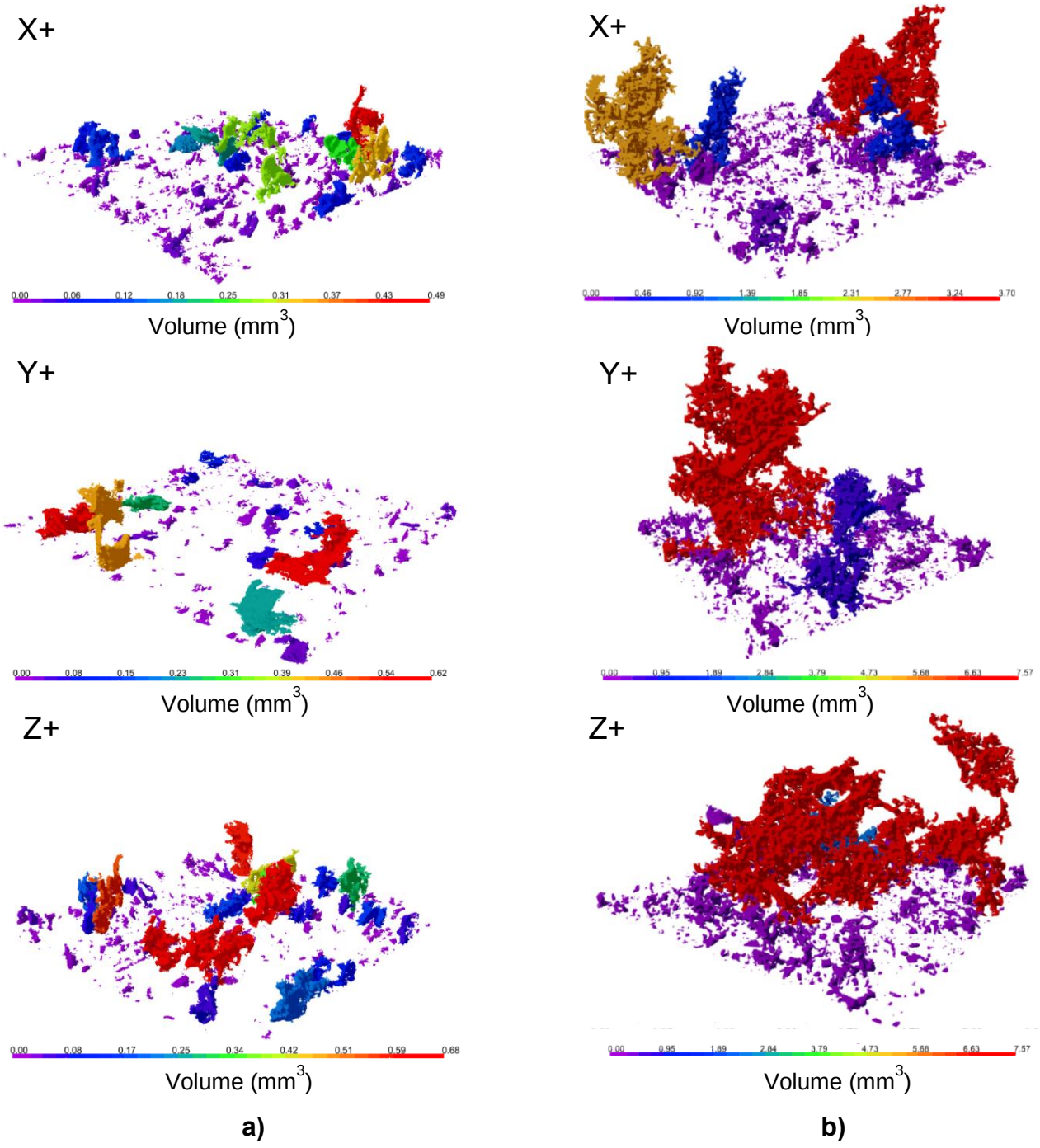


**Figure 6.** Volume renderings of the surface-connected porous networks for a) hot face A; b) hot face B, where the color indicates the volume of each individual network.

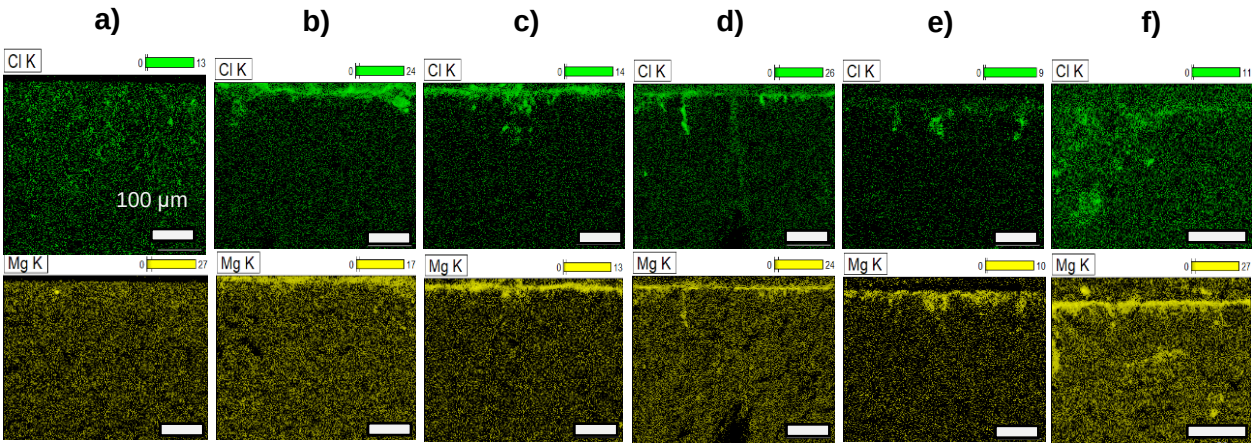


**Figure 7.** Salt permeation into hot face A as a function of time. EDS maps of Cl and Mg of cross sectioned native hot face A and hot face A immersed in molten chloride salt for 0, 50, 100, 500, 1000, and 3000 hours (a-f, respectively). Note that each data point is a different refractory sample. Salt permeation is measured as the depth of Cl into the bulk of the material.

The limited salt permeation is believed to be partly due to the formation of a secondary phase at the salt/refractory interface. In addition to the strong presence of surface magnesium in the EDS maps, X-ray diffraction confirms the formation of the magnesium silicate phase, forsterite ($Mg_2SiO_4$).

Figure 8 shows the X-ray diffractograms of virgin hot face A (a) and hot face A that has been immersed in salt for 3000 hours (b). The peaks in the virgin material correspond to alpha quartz and mullite phases. With immersion in molten chloride salt, the diffractogram reveal growth of a new crystal phase. The crosses (†) in Figure 8b denote the forsterite phase that has formed on the material due to contact with molten salt. The exposure of hot face A to molten salt also removes the amorphous content, which is present in the virgin hot face A.

Forsterite is the reported product of reactions involving $SiO_2$ and MgO with molten $MgCl_2$[14] and molten NaCl/KCl.[17] As a reference, a pure fused silica refractory was immersed in the ternary chloride salt for 50 hours at 720 °C, in order to evaluate the importance of both the polydispersity and presence of amorphous content in hot face A. XRD analysis showed no evidence of forsterite formation on the material surface, indicating the particular composition of hot face A (heterogenous with amorphous content) is required to form forsterite (Figure S5). In a second reference experiment, hot face A was immersed in molten NaCl/KCl binary at 720 °C for 50 hours. Similarly, no evidence of forsterite was observed in XRD analysis, which suggests that the presence of $MgCl_2$ is also critical to facilitate forsterite formation (Figure S6).

Cross-sectioned samples highlight the formation of surface forsterite but lack the spatial resolution to qualify the extent of the secondary phase on the sample. Scanning acoustic microscopy was used to compare the entire surface (nominally 13 mm x 13 mm) of an untreated hot face A coupon and a coupon after immersion in molten salt for 3000 hours (Figure 8c and d). The surface of the treated sample displays more condensed grey space, which indicates a greater surface coverage and fewer porous regions extending into the material bulk. This hypothesis is further reinforced by the corresponded EDS magnesium maps of the untreated and treated coupons surfaces (Figure 8e and f). The

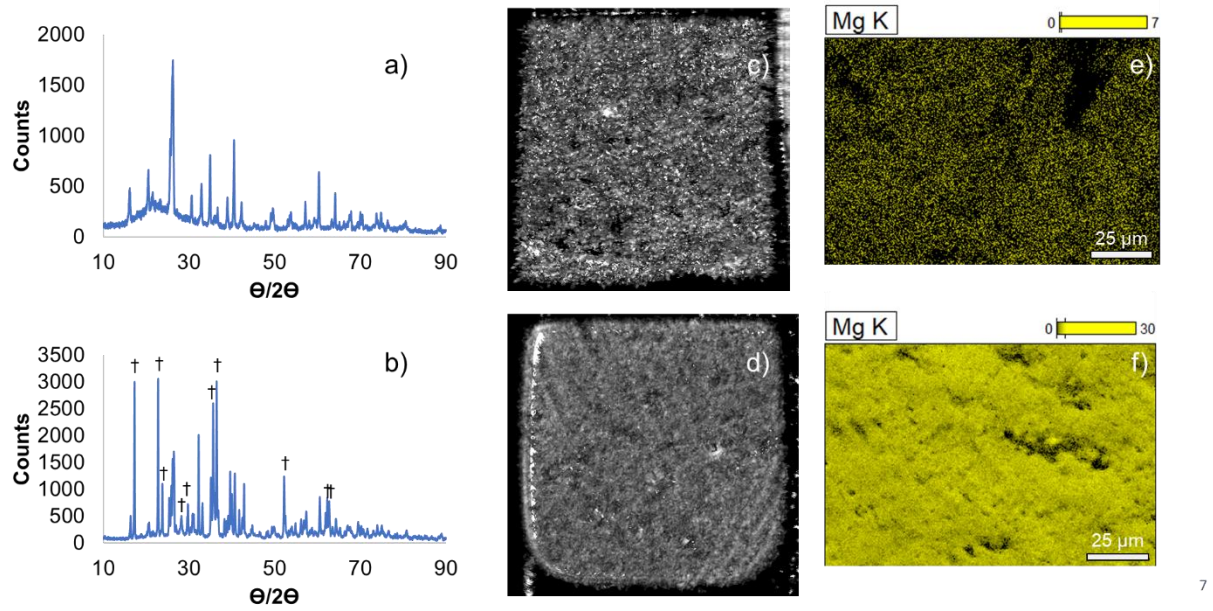


**Figure 8.** Virgin hot face A and hot face A immersed in salt for 3000 hours: X-ray diffractograms (a) and (b) respectively, scanning acoustic microscopy of coupon surfaces (c) and (d) respectively, and EDS Mg maps (e) and (f). The † symbols in the X-ray diffractogram of the 3000-hour immersed hot face A coupon highlight peaks that belong to the secondary phase that is formed on the material surface due to reaction with molten salt (forsterite, $Mg_2SiO_4$).

development of the forsterite layer creates broad magnesium deposits with fewer large pores than the untreated coupon.

The mechanical properties of hot face A were investigated to determine whether long-term exposure to molten salt and formation of surface forsterite affects the compressive strength. The brick has a reported cold crushing strength (CCS) of 114 MPa.

**Table 2.** Cold Crush Strength (CCS) of native Hot Face A and Hot Face A after immersion in molten chloride salt for 3000 continuous hours. Student's t test performed*

| **Hot Face- Native** | | **Hot Face A- 3000 h** | |
|---|---|---|---|
| **Sample Number** | **CCS (MPa)** | **Sample number** | **CCS (MPa)** |
| 1 | 111.8 | 1 | 116.5 |
| 2 | 109.9 | 2 | 103.0 |
| 3 | 119.9 | 3 | 115.3 |
| 4 | 101.2 | 4 | 120.4 |
| 5 | 123.2 | | |
| ***Mean*** | *113.2* | ***Mean*** | *113.8* |
| ***StDev*** | *8.7* | ***StDev*** | *7.5* |

* t-value = 0.05, critical value = 1.895. t-value < critical value. Data are not statistically different

Table 2 shows the data generated from mechanical compression testing. The average and standard deviation of the virgin and immersed specimens were 113.2 MPa ± 8.7 MPa and 113.8 MPa ± 7.5 MPa. Student's t test was performed on the data to determine any statistical differences in the data set within 95% confidence. The t-value and critical value for a one-tailed test with a 95% confidence interval were 0.05 and 1.895, respectively. As the t-value is less than the critical value, the data was deemed to not be statistically different and indicated that long-term exposure and secondary phase formation of forsterite on the material surface do not affect mechanical compatibility of hot face A with molten chloride salt.

For comparison, an insulting firebrick (IFB) was subjected to similar mechanical testing. Should molten salt permeate through the hot face refractory layer, the IFB will become wetted with salt. The virgin material was measured to have a CCS of 0.97 MPa ± 0.08 MPa, which is within the CCS reported by the manufacturer (1.00 MPa). Three samples were then immersed in salt for 50 hours at 720 °C. The high porosity (>80%) of the material results in the open pores being filled with salt. The CCS of the salt-wetted IFB decreased dramatically to 0.05 MPa ± 0.07 MPa, clearly demonstrating the deleterious impact of salt contact. This study further emphasizes the need to prevent the salt from permeating through the hot face and contacting the insulation layer(s).

While hot face A demonstrates adequate thermal, chemical, and mechanical stability in molten salt, the chemical composition of the salt does not remain consistent throughout long-duration testing. An aliquot of salt was extracted after the conclusion of each 50-, 100-, 500-, and 1000-hour experiment and submitted for elemental analysis via inductively coupled plasma - optical emission spectrometry (ICP-OES). Figure 9 shows the normalized wt% of the ternary salt. Detailed salt composition and trace ceramic constituents that come from chemical dissolution of the refractory are shown in Table S3.

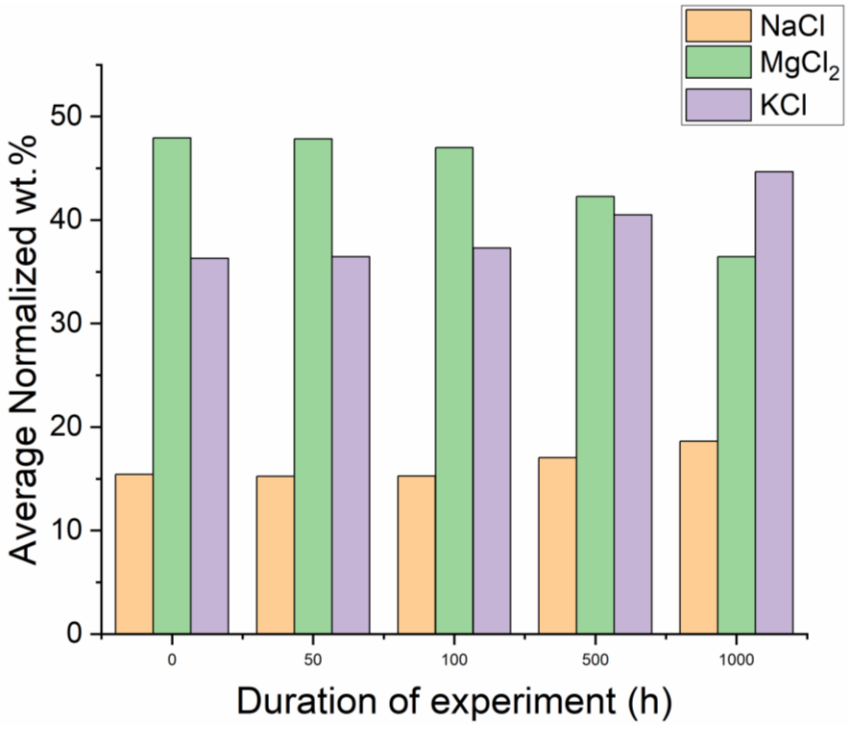


**Figure 9.** Normalized wt% of salt composition after chemical compatibility testing.

There is evidence of chemical dissolution of the refractory (Fe and Si) into the salt after 1000 hours of exposure (Table S3). However, the concentrations of refractory elements do not exceed 0.1 wt%, beyond which it is believed that the solubilized refractory will affect the thermophysical properties of the salt. Moreover, low concentrations of refractory components in the salt indicate the secondary phase is adherent to the refractory surface and less susceptible to chemical dissolution.

An unexpected observation from the ICP-OES data was the steady relative decrease in $MgCl_2$ and corresponding relative increase in NaCl and KCl concentration, indicating loss of $MgCl_2$. $MgCl_2$ concentration decreases from 47.9 wt% in pure salt to 36.4 wt% in salt after 1000 hours of testing (Figure 9). The formation of the magnesium silicate secondary phase was initially suspected as the cause of the $MgCl_2$ decrease. However, accounting for surface area and depth of forsterite phase in the refractory coupons, the loss of $MgCl_2$ due to forsterite formation was calculated to be approximately 3.2 wt%. This is considered to be an absolute maximum, as the calculation assumes a complete surface coverage of forsterite with uniform thickness that is 100% dense. Nevertheless, forsterite formation alone does not fully account for the loss of $MgCl_2$ from the system.

Composition changes in the salt may be due to multiple factors, including salt evaporation and/or salt instability. The ternary chloride salt does have a measurable vapor pressure. However, the chemical composition of the vapor is unknown, and therefore it is unclear whether the vapor is comprised equally or unequally of the three salt constituents. Any compositional changes due to salt/liner interaction should be less pronounced on the commercial scale, as compared to laboratory-scale experiments. Large salt tanks will contain orders of magnitude more salt volume per surface area of exposed refractory material. In short, future study of this system should involve the investigation of salt stability and salt containment with refractory liners in a larger tank demonstration. This would provide chloride salt data on a scale that is more representative of a full industrial system.

## Conclusions

A refractory internal liner is proposed to protect the steel walls of molten chloride salt thermal energy storage tanks for CSP applications. The refractory liners in industrial molten chloride electrolysis cells provide a good initial design point, but the different conditions and requirements of CSP present new and unique challenges. Without careful consideration of refractory properties, such as wettability, thermal expansion, and heat capacity; a salt freeze/thaw cycle may occur in the liner, which may crack the liner leading to failure of the tank. Preventing ingress of the salt is achieved by selecting a low-porosity hot face refractory that exhibits chemical stability in the presence of the salt.

Aluminosilicate candidates, similar in composition to those used in the magnesium industry, were screened. The down-selected material was tested isothermally at 720 °C in the molten chloride salt for up to 3000 hours. The penetration of the salt is characterized via SEM. Elemental mapping by EDS shows a penetration layer on the hot face material at a depth of approximately 20 μm. Apart from native cracks in the material, there is no significant penetration of the salt beyond this point. X-ray CT showed that the down-

selected refractory showed very little ingressed salt across millimeter dimensions and suggested that secondary phase formation was the reason as opposed to a lack of surface-connected porosity. XRD analysis compared the crystal phases of the virgin and salt-exposed material. XRD performed on the salt-exposed material suggested the formation of a secondary forsterite phase, which is reported to have high thermal stability and low corrosion in molten alkali chloride salt and may act as a protective barrier to further salt ingress. This secondary phase, however, does not adversely affect the mechanical properties of the material. Chemical composition of the post-test salt did not detect refractory components in the salt at significant concentrations, which indicates that hot face A and the secondary surface phase are chemically stable in the salt. However, extended refractory-salt contact leads to a selective decrease in $MgCl_2$ concentration. This must be accounted for in the system design and will be the focus of further study to determine its severity at larger scales.

## Acknowledgements

This work was authored in part by the National Renewable Energy Laboratory, operated by Alliance for Sustainable Energy, LLC, for the U.S. Department of Energy (DOE) under Subcontract ADJ-9-92133-01 under Prime Contract No. DE-AC36-08GO28308. Funding provided by DOE Office of Energy Efficiency and Renewable Energy (EERE). The views expressed in the article do not necessarily represent the views of the DOE or the U.S. Government. The publisher, by accepting the article for publication, acknowledges that the U.S. Government retains a nonexclusive, paid-up, irrevocable, worldwide license to publish or reproduce the published form of this work, or allow others to do so, for U.S. Government purposes. The authors gratefully acknowledge Ms. Thao Truong, Mr. Douglas DeVoto, and Mr. Joshua Major for their contributions.

The research leading to the X-ray CT results received funding from the Engineering & Physical Sciences Research Council (EPSRC) *via* grants EP/P009050/1 and EP/M028100/1. P. R. S. acknowledges the support of the Royal Academy of Engineering (CIET 1718/59).

## References

[1] M. Mehos, C. Turchi, J. Vidal, M. Wagner, Z. Ma, C. Ho, C. Andraka, A. Kruizenga, A concentrating solar power Gen3 demonstration roadmap. *NREL/TP-5500-67464* **2017**.

[2] S. Gage, C. Kimbal, J. Dupree, J. Rigby, C. Turchi, Technical performance of refractory liners for molten chloride salt thermal energy storage systems. SolarPACES 2020, Virtual Event. September 28 - October 2, **2020**.

[3] G. Shekhovtsov, V. Shchegolev, V. Devyatkin, A. Tatakin, I. Zabelin, in *Essential Readings in Magnesium Technology* (Eds.: S.N. Mathaudhu, A.A. Luo, N.R. Neelameggham, E.A. Nyberg, W.H. Sillekens), Springer International Publishing, Cham, **2016**, pp. 97–100.

[4] Y. Grosu, U. Nithiyanantham, A. Zaki, A. Faik, *npj Materials Degradation* **2018**, *2*, 34.

[5] Y. Grosu, N. Udayashankar, O. Bondarchuk, L. González-Fernández, A. Faik, *Solar Energy Materials and Solar Cells* **2018**, *178*, 91.

[6] W. Ding, A. Bonk, T. Bauer, *AIP Conference Proceedings* **2019**, *2126*, 200014.

[7] J. C. Gomez-Vidal, *npj Materials Degradation* **2017**, *1*, 7.
[8] W. E. Lee, S. Zhang, *International Materials Reviews* **1999**, *44*, 77.
[9] N. S. Jacobson, K. N. Lee, T. Yoshio, *Journal of the American Ceramic Society* **1996**, *79*, 2161.
[10] S. Zhang, W. E. Lee, *Journal of the European Ceramic Society* **2001**, *21*, 2393.
[11] H. Wang, B. Glaser, D. Sichen, *Metallurgical and Materials Transactions B* **2015**, *46*, 749.
[12] T. Kimura, in *Advances in Ceramics - Synthesis and Characterization, Processing and Specific Applications*, **2011**.
[13] X. Liu, N. Fechler, M. Antonietti, *Chemical Society Reviews* **2013**, *42*, 8237.
[14] E. I. Cooper, D. H. Kohn, *Ceramics International* **1983**, *9*, 68.
[15] S. Zhang, D. D. Jayaseelan, G. Bhattacharya, W. E. Lee, *Journal of the American Ceramic Society* **2006**, *89*, 1724.
[16] H.-T. Sun, M. Fujii, N. Nitta, M. Mizuhata, H. Yasuda, S. Deki, S. Hayashi, *Journal of the American Ceramic Society* **2009**, *92*, 962.
[17] Z. F. Wang, M. J. Chen, Y. Ma, H. Liu, C. H. Han, X. T. Wang, *International Journal of Applied Ceramic Technology* **2017**, *14*, 3.
[18] J. Takahashi, Y. Kawai, S. Shimada, *Journal of the European Ceramic Society* **1998**, *18*, 1121.
[19] A. Saberi, Z. Negahdari, B. Alinejad, F. Golestani-Fard, *Ceramics International* **2009**, *35*, 1705.
[20] L. Chen, G. Ye, Q. Wang, B. Blanpain, A. Malfliet, M. Guo, *Ceramics International* **2015**, *41*, 2234.
[21] K. J. Brondyke, *Journal of the American Ceramic Society* **1953**, *36*, 171.
[22] *ASTM C621-09(2018), Standard Test Method for Isothermal Corrosion Resistance of Refractories to Molten Glass*, West Conshohocken, PA, **2018**.
[23] Y. Zhao, J. Vidal, *Solar Energy Materials and Solar Cells* **2020**, *215*, 110663.
[24] N. Klammer, C. Engtrakul, Y. Zhao, Y. Wu, J. Vidal, *Anal. Chem.* **2020**, *92*, 3598.
[25] *ASTM C133-97(2015), Standard Test Methods for Cold Crushing Strength and Modulus of Rupture of Refractories*, West Conshohocken, PA, **2015**.
[26] A. Rabbani, S. Jamshidi, S. Salehi, *Journal of Petroleum Science and Engineering* **2014**, *123*, 164.